Geological Characteristics of Von Kármán Crater, Northwestern South Pole-Aitken Basin: Chang'E-4 Landing Site Region

Jun Huang[1], Zhiyong Xiao[1], Jessica Flahaut[2,3], Mélissa Martinot[4,5], James Head[6], Xiao Xiao[1], Minggang Xie[7], Long Xiao[1]

[1] State Key Laboratory of Geological Processes and Mineral Resources, Planetary Science Institute, School of Earth Sciences, China University of Geosciences, Wuhan 430074, China

[2] CRPG-CNRS/Université de Lorraine, 54500 Vandœuvre-lès-Nancy, France

[3] IRAP-CNRS-CNES/Université Paul Sabatier, 31400 Toulouse, France

[4] Faculty of Science, Vrije Universiteit Amsterdam, Amsterdam, The Netherlands

[5] Université Lyon 1, ENS-Lyon, CNRS, UMR 5276 LGL-TPE, Villeurbanne, France

[6] Department of Earth, Environmental and Planetary Sciences, Brown University, Providence, RI, 02912 USA

[7] Space Science Institute, Macau University of Science and Technology, Macau, China

Corresponding author: Jun Huang (junhuang@cug.edu.cn)

Key Points:

- We report a detailed 3D geological analysis of the nature and history of pre-Nectarian aged Von Kármán Crater in the lunar South Pole-Aitken basin.
- The region contains farside mare basalts affected by linear features and ejecta material from a wide range of surrounding craters.
- Our geological analysis provides a framework for the Chang'E-4 mission to carry out in-situ exploration.

This article has been accepted for publication and undergone full peer review but has not been through the copyediting, typesetting, pagination and proofreading process which may lead to differences between this version and the Version of Record. Please cite this article as doi: 10.1029/2018JE005577

Abstract

Von Kármán crater (diameter =~186 km), lying in the northwestern South Pole-Aitken basin, was formed in the pre-Nectarian. The Von Kármán crater floor was subsequently flooded with one or several generations of mare basalts during the Imbrian period. Numerous subsequent impact craters in the surrounding region delivered ejecta to the floor, together forming a rich sample of the SPA basin and farside geologic history. We studied in detail the targeted landing region (45.0–46.0°S, 176.4–178.8°E) of the 2018 Chinese lunar mission Chang'E-4, within the Von Kármán crater. The topography of the landing region is generally flat at a baseline of ~60 m. Secondary craters and ejecta materials have covered most of the mare unit, and can be traced back to at least four source craters (Finsen, Von Kármán L, Von Kármán L' and Antoniadi) based on preferential spatial orientations and crosscutting relationships. Extensive sinuous ridges and troughs are identified spatially related to *Ba Jie* crater (diameter = ~4 km). Reflectance spectral variations due to difference in both composition and physical properties are observed among the ejecta from various-sized craters on the mare unit. The composition trends were used together with crater scaling relationships and estimates of regolith thickness to reconstruct the subsurface stratigraphy. The results reveal a complex geological history of the landing region, and set the framework for the in-situ measurements of the CE-4 mission, which will provide unique insights into the compositions of farside mare basalt, SPA compositional zone, including SPA compositional anomaly and Mg-pyroxene annulus, regolith evolution and the lunar space environment.

Plain Language Summary

The South Pole-Aitken (SPA) basin on the farside of the Moon is the largest known impact structure in the solar system. It is the key area to answer several important questions about the Moon, including its internal structure and thermal evolution. We outline the geologic history of an important area (Von Kármán crater) within SPA. In 2018, a new Chinese lunar mission Chang'E-4 (CE-4) will be the first to land in the Von Kármán crater, within the SPA basin. The scientific instruments of CE-4, mounted on a lander and a rover, will analyse both surface and subsurface of this farside region. Here we present a detailed geological study of the selected landing region of CE-4, based on remote sensing data of the Moon. Our study identified several targets of high scientific interests and proposes testable hypotheses for the CE-4 mission.

1 Introduction

The farside South Pole-Aitken (SPA) basin is the largest known impact structure on the Moon (Stuart-Alexander, 1978; Wilhelms et al., 1987). Its geology provides insights into the composition of the lower crust and upper mantle, the impact flux in early lunar history, the nature and evolution of basin-scale impact melt deposits, and the nature of large impact basins and their formation and modification processes (Head et al., 1993; Spudis et al., 1994; Garrick-Bethell & Zuber, 2009; Potter, Collins, Kiefer, McGovern, & Kring, 2012; Vaughan & Head, 2014; Moriarty and Pieters, 2018). The SPA basin has been studied with spectral observations (e.g. Pieters et al., 2001; Ohtake et al., 2014) and recently been subdivided into four distinct compositional zones based on Moon Mineralogy Mapper (M^3) data (Moriarty and Pieters, 2018): 1) a central ~700 km wide SPA compositional anomaly (SPACA), which exhibits a strong Ca-pyroxene signature, which is different from typical mare basalts, 2) a Mg-Pyroxene Annulus, which is characterized by Mg-rich pyroxenes, 3) a Heterogeneous Annulus, which exhibits mixing of localized pyroxene-rich units and feldspathic materials, and 4) the SPA Exterior, which is mafic-free and dominated by feldspathic materials. Pyroxene compositions in both the Heterogeneous Annulus and Mg-Pyroxene Annulus are similar. Moriarty and Pieters (2018) has indicated that the Mg-pyroxene unit is beneath the SPACA Ca-pyroxene unit from the stratigraphic relationships and central peak exposures among craters within SPACA. The material of Mg-Pyroxene Annulus was the main material excavated and melted by the SPA-forming event due to the relatively uniform composition and the great area, depth and thickness of the Mg-Pyroxene Annulus. The extremely large size of the SPA basin strongly suggests that it has excavated sub-crustal and mantle material (e.g. Melosh et al., 2017); however, the lack of evidence for widespread dunite or olivine-dominated mineral assemblages, and the dominance of Mg-pyroxenes in the basin interior, suggest that lunar mantle must include a significant Mg-pyroxene component (Moriarty and Pieters, 2018).

Von Kármán crater (diameter *D*=186 km; central coordinates as 44.4°S 176.2°E) (Fig. 1a) lies within the Mg-Pyroxene Annulus, just northwest of the SPACA terrain. This crater is a pre-Nectarian crater (Losiak et al., 2009; Yingst et al., 2017), younger than the Von Kármán M basin (*D*=219 km; central coordinates as 49.4°S, 174.9°E), and older than the Leibnitz crater (diameter *D*=236 km; central coordinates as 38.2°S 179.3°E: Figs. 1b and 1c) (Yingst et al., 2017). Mare basalts flooded parts of the Von Kármán crater floor during the Imbrian Period (Wilhelms, Howard, & Wilshire, 1979; Yingst & Head, 1997; Yingst et al., 2017; Pasckert, Hiesinger, & van der Bogert, 2018), but a portion of the central peak remains exposed near the center of the crater (Fig. 1d). Finsen crater (diameter *D*=73 km; central coordinates as 42.3°S 182.3°E), Von Kármán L crater (diameter *D*=29 km; central coordinates as 47.8°S 177.9°E) and a similar-sized unnamed crater nearby (we informally denote it as Von Kármán L' in this study) were formed subsequent to the Von Kármán crater (Wilhelms et al., 1979)(Fig. 1c). Relatively higher albedo linear features on the mare basalt of Von Kármán crater converge towards the crater Finsen (Fig. 1b), which is located within the SPACA, suggesting that the SPACA material has been derived from Finsen crater.

In 2018, the Chinese lunar mission Chang'E-4 (CE-4) (Wu et al., 2017) will explore the SPA basin. It will be the first in-situ exploration of the farside of the Moon. The selected landing region for CE-4 (45°S - 46°S, 176.4°E - 178.8°E) (Wu et al., 2017) is located on the southern floor of the Von Kármán crater. In-situ exploration within the Von Kármán landing region will bring unprecedented imaging, spectral, radar and low-frequency radio spectral data for the landing region, and it will greatly improve our understanding about the compositions of farside mare basalt, SPA compositional zones including SPA compositional anomaly and Mg-pyroxene annulus, regolith evolution and the lunar space environment. Indeed, the U.S. National Research Council (2007) has identified key scientific priorities for future lunar exploration that can be addressed from the Von Kármán crater, including the

possibility to study the existence and extent of differentiation of the SPA melt sheet (Morrison et al., 1998; Nakamura et al., 2009; Vaughan and Head, 2014) and possible exposed upper mantle materials (Melosh et al., 2017; Moriarty and Pieters, 2018). In this study, we have 1) investigated the geological characteristics of the landing region using available remote sensing data including topography, high-resolution imaging, and reflectance spectral data, 2) identified targets of high scientific interests, and 3) proposed testable hypothesis for the CE-4 mission.

2 Methods

2.1 Datasets

We analyzed the local geology using the Lunar Reconnaissance Orbiter Camera (LROC) Wide Angle Camera (WAC) mosaic (100 m/pix) for regional context (Robinson et al., 2010), Kaguya Multiband Imager (MI) 750 nm reflectance mosaic (14 m/pix) for albedo variations (Ohtake et al., 2008), Terrain Camera (TC) morning mosaic (7 m/pix) for local context (Kato et al., 2010), and LROC Narrow Angle Camera (NAC) images (0.5-1.6 m/pix) for small geological feature identification. Topographic analyses were performed using the merged Digital Elevation Model (DEM) that is derived from the LRO Lunar Orbiter Laser Altimeter (LOLA) (Smith et al., 2010) and Kaguya TC data (SLDEM: 59 m/pix) (Barker et al., 2016). We produced a slope map for the landing region using SLDEM at a 59 m scale.

2.2 Regolith and ejecta thicknesses

We estimated the thickness of the regolith within the proposed landing area using NAC images that have incidence angles less than 55° following the method described in Quaide and Oberbeck (1968). Quaide and Oberbeck (1968) found that relatively fresh concentric craters with diameters less than 250 meters could be used to estimate the thickness of the

regolith with the equation: thickness = (k - D_F / D_A) * D_A * tan(α) / 2, where D_A is the rim-to-rim diameter of a crater, D_F is the diameter of the inner concentric ring, k is an empirically constant, and α is the angle of repose of materials on the surface of the Moon. The angle of repose of lunar regolith (α) is 31°, so the corresponding k is 0.86 and the corresponding slope of inner walls of fresh craters is 31° ± 2° (Quaide & Oberbeck, 1968). It is considered more robust to identify concentric craters using images with smaller incidence angle, otherwise the flat bottomed craters and concentric craters could be misrecognized as normal craters and flat-bottomed craters, respectively (Fa et al., 2014). Thus, we conservatively chose these LROC NAC images with incidence angles less than 55°. Only relatively well-preserved craters with diameters less than 250 meters were used to estimate the regolith thickness (Oberbeck & Quaide, 1967) due to the difficulties in diameter identification and measurements using degraded craters (Soderblom, 1970).

The thickness of ejecta deposits (i.e., the mixture of ejecta and excavated local material) that were transported from craters outside of the landing region are estimated using the empirical scaling laws estimated by Xie and Zhu (2016). Local geological context suggests that the Finsen, Von Kármán L, and Von Kármán L' craters have contributed most of the ejecta deposits within the proposed landing region (McGetchin et al., 1973; Oberbeck et al., 1975; Petro and Pieters, 2006; Sharpton, 2014). We have a detailed description of the model in section 4.4.

2.3 Absolute model ages

The absolute model age of the landing region is derived from crater statistics. Since obvious secondary craters (i.e., secondaries) that occur in chains and clusters have almost covered the entire landing region (see section 3.2), we employed two independent methods to estimate the model age. 1) The mare surface on the floor of Von Kármán was interpreted to

be emplaced by one episode of basaltic volcanism based on the uniform reflectance spectral characteristics (Yingst & Head, 1999). Therefore, the model age for the mare surface is derived via craters that are substantially larger than the largest obvious secondaries (diameter D>~2 km; see section 3.1) on the LROC WAC mosaic. 2) There are a few subareas, including two within the proposed landing region of Chang'E-4, where craters larger than ~300 – 400 m are not heavily modified by obvious secondaries. The model ages for these subareas are derived by studying the size-frequency distributions of craters larger than 300 – 400 m in diameter using Kaguya TC mosaics. During analysis of the crater statistics, the CraterTools toolbox in ArcMap was employed to collect the craters by fitting circles based on three points on the crater rims. The crater chronology and production functions proposed by Neukum et al. (2001) were used to derive the model ages based on the Poisson Possibility analyses method advocated by Michael et al. (2016).

2.4 Compositional aspects

In order to distinguish geological units of different composition, age, or texture, a RGB composite mosaic of MI data was built (R = 750 nm/415 nm, G = 950 nm/750 nm, B = 415 nm/750 nm (e.g. Weitz and Head, 1999; Huang et al., 2011). Observed variations in this RGB composite that mimic the Clementine false color ratio are commonly due to variations of the titanium and iron contents and the maturity of the surface materials (Pieters et al., 1993). We marked locations representative of different spectral units in the MI RGB composite. The mineralogy of these locations was derived from spectroscopic data from Chandrayaan-1 Moon Mineralogy Mapper (M^3) instrument (Pieters et al., 2009). M^3 is a visible to near-infrared hyperspectral imager, with 85 spectral channels spanning from 430 to 3000 nm. The data used in this study are archived in the Planetary Data System (PDS, version 1 of Level 2), radiometrically corrected (Green et al., 2011), geometrically corrected (Boardman et al.,

2011), thermally corrected (Clark et al., 2011), and photometrically corrected (Besse et al., 2013). The optical period used in this study is the OP2C2, with a resolution of 280 m/pix. We selected this optical period because it covers the entire landing site region. The continuum of the spectra was removed with the algorithm developed by Martinot et al. (2018), and a suite of band parameters were calculated. The continuum is modeled as linear segments connected to the original M^3 spectrum in points called tie points, defined in fixed intervals. The algorithm maximized the 1 and 2 micron absorption band areas and automatically extracted the continuum. After continuum removal, a suite of spectral parameters is calculated (e.g., band center position, band area, band depth) and exported as maps.

3 Results

3.1 Surface morphology and terrain characteristics

The selected landing region is located on the mare units within Von Kármán crater. The average elevation of this area is about -5926 m, with a standard deviation of 20.4 m. The elevation ranges over about 321 m. The highest geological feature in the region is the mound located near the north boundary (Fig.2a). The proposed landing region is generally flat at a scale length of 59 m, as nearly 99% of the area has a slope less than 15°, and the slopes of about 94% of the area are less than 5° at a 59 m scale length (Fig.2b). Local steep slopes (>15°) are mostly associated with craters larger than ~1 km diameter (Fig. 2b). The northeastern and southwestern portions of the landing area are lower in elevation compared with the northwestern and southeastern portions (Fig. 2a). NE–SW linear features with elevated topography are visible across the landing region (Fig. 2) and correspond to the ejecta deposits and secondary craters that originated from the Finsen crater (Fig. 1b).

Obvious secondary craters are widespread within the entire landing region (Fig. 3a). With irregular planar morphology, secondaries are recognized by their spatial occurrences in chains and/or clusters that exhibit herringbone-shaped morphology. Secondaries within a given chain and cluster have similar preservation states and their elevated crater rims all point in the a same direction. Based on the preferential spatial orientation of secondaries within the landing region (Fig. 1d and Fig. 3), we have identified at least four sets of various-sized secondary craters that have different preservation states. The NE – SW trending secondary craters (Fig. 3a) are larger than 500 m in diameter, and they converge toward the Finsen crater (Fig. 1b and Fig. 3a). These secondaries are heavily degraded because their rims now occur as sub-parallel ridges (Fig. 3b) and the original shallow cavity has been gradually filled by mass wasting and subsequent ejecta deposition. The second set of secondaries generally trend north to south, and are larger than 1 km in diameter. The secondaries overlap those formed by Finsen and have a better preservation state (Fig. 3c and Fig. S1). The steepened crater walls are located at the southern part of the secondaries, suggesting that the source crater is located to the south of Von Kármán. The minimum diameter of the parent crater should be at least 20 km considering that the maximum ratio between continuous secondaries and primaries is ~5% on terrestrial planets (Melosh, 1989), and that distant secondaries are much smaller than those on continuous secondaries facies (Xiao, 2016). Tracing southward along a great ellipse circle in ArcMap, we noticed that the Antoniadi crater (D=138 km; central coordinates as 69.3°S, 186.9°E) is the most likely source crater that fulfills the above criteria (Fig. S1). Judging by the same criteria, the freshest secondaries within the proposed landing region are the east–northeast and south–southwest trending secondaries that are located on top of the secondaries formed by Finsen and Antoniadi. These secondaries (e.g., Fig. 3d) are much smaller and they are ~250–500 m in diameter (Fig. 3d). Tracing along the

secondaries we find that the Von Kármán L and Von Kármán L' craters to the south of the landing region are the possible source craters (Fig. S2).

Notably, we have identified extensive sinuous ridges within the landing region, which are different from wrinkle ridges (e.g., Binder, 1982) and degraded secondary crater chains (e.g., Lucchitta, 1977) on the Moon. The ridges are asymmetric in shape and extend in a sinusoidal-like shape (Fig. 4a): the widths of the ridges are tens of meters. Sinuous troughs are formed between the ridges (Fig. 4b), and both the troughs and ridges are spatially associated with *Ba Jie* crater, which is to the west of the landing region (Fig. 4c).

3.2 Compositional diversity

Variations in composition are identified in the reflectance spectra of the proposed landing area (Fig. 5). Spectrally, the entire region is dominated by pyroxene signatures (Fig. 5b, Fig. 5d and Fig. 5e). Pyroxene reflectance spectra are characterized by the presence of diagnostic, broad absorption bands located around 1 and 2 microns, shifting towards longer wavelengths with increasing iron or calcium content (e.g., Klima *et al*., 2007). The 1 and 2 micron absorption band center positions, displayed on the parameter maps, show that the mare itself is rather homogenous (Fig. 5b). Minor variations of the 1 and 2 micron absorption band centers positions of pyroxene spectra are observed within impact crater ejecta located on the mare floor, suggesting variations in chemistry with depth (Fig. 5b). On the MI color composite (Fig. 5d), relatively fresh small craters (diameter ~66 to 324 m) (Fig. 6a) show blue-toned ejecta (e.g., site 1 in Fig. 5d) and higher albedo in the MI 750 nm reflectance data (Fig. 5c). Their reflectance spectra are consistent with that of Low-Calcium Pyroxene (LCP)-bearing material (Fig. 5e). The orange-toned ejecta (e.g., site 2 in Fig. 5d) are related to larger craters (diameter 252–950 m) (Fig. 6b), with spectra consistent with Higher-Calcium

Pyroxene (HCP)-bearing materials (Fig. 5e). The spectra of the ejecta of *Ba Jie* crater are similar to the spectra of the orange-toned ejecta (sites 4, 5, 6, and 7 in Fig. 5d). The ejecta on the rim of *Ba Jie* crater presents HCP signatures, but with larger spectral contrast (site 5 in Fig. 5d). The mare itself (site 3 in Fig. 5d) has a spectral signature consistent with these HCP-rich materials with weaker absorption bands.

3.3 Regolith thickness

We analyzed relatively fresh concentric impact craters using LROC NAC images with incidence angle less than 55° to estimate the regolith thickness using the method of Quaide and Oberbeck (1968). These images have solar angles greater than 35°, which are larger than the repose angle of the regolith (31°). Therefore, we can clearly determine the morphology of the impact craters with these NAC images (Fa et al., 2014). The estimated thickness of the regolith in this area varies from ~2.5 m to 7.5 m (Fig.7). It appears that the regolith in the northeastern portion of the region is thicker than that of the southwestern portion, which is consistent with a larger contribution of ejecta deposits (Fig. 10), as well as a strong gardening effect of secondary crater chains (Fig. 2a) formed as a result of the Finsen crater-forming event.

3. Stratigraphic ages of the landing area

Obvious secondary crater chains have dominated the entire mare unit on the floor of Von Kármán (Fig. 3a). Most of the secondaries are less than 2 km in diameter (section 3.2). Therefore, we studied the size-frequency distribution of craters larger than 2 km in diameter to estimate the model age of the mare unit. The absolute model age derived by probability analyses (Michael, Kneissl, & Neesemann, 2016) is 3.6 (+.09, -.2) Ga, which falls in the Imbrian period. This result is consistent with the recent geological mapping (Yingst et al.,

2017), and crater statistics (Haruyama et al., 2009). We also selected three sub-regions on the mare units that have been less affected by large secondary craters in order to verify the model age. Fig. 8a shows the locations of the counting areas. The surface morphology of the sub-regions shows that craters larger than ~300 – 400 m are not obvious secondary craters (e.g., Figs. 8c, 8e, 8g), and model ages derived from the crater counts are identical with those estimated from craters larger than 2 km in diameter.

4 Discussion

4.1 Context of CE-4 Mission

CE-4 is scheduled to launch in 2018 and will be the first lunar farside in-situ exploration mission. The CE-4 mission will be carried out in two phases. First, a relay satellite with two micro-satellites will be launched by a CZ-4C rocket from Xichang, China. The relay satellite will be sent to the Earth-Moon Lagrange Point 2. A Dutch-made low-frequency radio spectrometer (0.1 – 80 MHz) is carried by the relay satellite to perform space physics measurements. In addition, the relay satellite will carry several laser reflectors for assisting orbital determination. This mission will also include two-micro satellites that will orbit the Moon, and they will be equipped with very-long-baseline interferometry (VLBI) instruments to conduct radio science experiments. One of the micro satellites will have a visible wavelength micro camera contributed from Saudi Arabia. Six months after the launch, the second part of the CE-4 mission, which is comprised of a lander and a rover, will be launched by a CZ-3B rocket launched from Xichang, China. Since both the lander and the rover were designed as a backup for the Chang'E-3 mission, some of the science payloads on Chang'E-4 are similar to those on Chang'E-3 (Jia et al., 2018), which include a landing camera, a terrain camera, a panorama camera on the lander and a visible/near infrared imaging spectrometer (He et al., 2014), and two ground penetrating radars (Fang et al., 2014) on the rover.

Additional instruments on the lander (Jia et al., 2018) include 1) a low-frequency radio spectrometer (0.1 – 40 MHz) to perform joint space physics observations with the low-frequency radio spectrometer on the relay satellite, 2) a German lunar neutron and radiation dose detector to explore the farside surface radioactive environment, and 3) a lunar micro ecosystem for astrobiology experiments and public outreach. A new instrument on the rover (Jia et al., 2018) is the Swedish neutral atom detector designed to study the interaction between the solar wind and lunar surface materials. However, the CE-4 will not be equipped with the alpha particle x-ray spectrometer that was previously used by CE-3 to detect elemental abundances within surface material (Wu et al., 2017, Jia et al., 2018). Still the lander and rover together should be able to perform imaging, spectral, radar and low-frequency radio spectral measurements.

4.2 Geological features

Several features of interest have been identified within the landing region, including farside mare basalts, sinuous linear features and ejecta rays. Non-nearside mare basalts will be investigated in situ for the first time at Von Kármán and may bring new clues about the farside and SPA volcanism. Spectral data show HCP signatures associated with the mare unit, which is consistent with most lunar mare (e.g., Staid et al., 2011). However, in contrast to the Chang'E-3 landing site, olivine has not yet been detected at Von Kármán (Ling et al., 2015; Zhang et al., 2015), which suggests that the farside mare might be of slightly different composition. The mare unit is homogeneous and likely to represent a single eruptive episode during the lunar peak volcanic period that occurred in the Late Imbrian (3.80–3.20 Ga) (e.g., Yingst & Head, 1999). A single eruptive episode was one in which the mechanism of emplacement did not significantly vary over the period of activity, meaning

that the rock unit left in place should share generally similar morphological and compositional characteristics, making it a viable geologic unit.

Sinuous linear features, ridges and troughs, have been identified in the vicinity of *Ba Jie* crater. They are distinct from lunar wrinkle ridges, but their origin remains controversial. For example, Oberbeck (1975) proposed these to be ejecta deposits typical of small craters in which the ejecta is emplaced at relatively low velocity, and Atwood-Stone et al. (2017) suggested that these structure are likely the results of Kelvin-Helmholtz instabilities within the ejecta flows. The key information to understand their formation mechanism is the subsurface structure of these features, i.e., the depth and structural disturbance of the ejecta deposits of the *Ba Jie* crater, and whether or not fractures deeper than *Ba Jie*'s ejecta exist. The ground penetrating radars onboard CE-4 could reveal the subsurface structure of these linear features, and provide clues to their possible formation mechanism.

The secondary craters produced by the Finsen crater-forming event, and associated with relatively high albedo linear features, are heavily degraded but also of interest (Fig. 1b and Fig. 3). Hawke et al., (2004) proposed four different mechanisms to explain the formation of impact rays: 1) immature primary ejecta emplacement, 2) secondary craters immature local material deposition, (3) the action of debris surges downrange of secondary clusters, and (4) immature interior. Reflectance spectra for the landing region show that the rays formed by Finsen appear to have distinct composition compared with the buried mare basalts (Fig. 5b), indicating that the rays are composed of primary ejecta deposits. With the aid of the CE-4 cameras and radar system, the thickness and spatial distribution of impact ejecta from the Finsen crater could be more well constrained. This would be the first in-situ constraint for the subsurface structure of compositional rays, which will serve as an observational basis for understanding the efficiency of material transport by impact cratering on the Moon.

4.3 Stratigraphy of the landing region

Impact craters are probes of local stratigraphy (Melosh, 1989). Variations of reflectance spectra of crater ejecta deposits indicate vertical variations in composition/mineralogy in the landing area (section 3.3). We used the geometric relationship between the diameter of impact craters and the depth from which the ejecta was excavated to reconstruct the regional stratigraphy (Fig. 9). The maximum depth of excavation is approximately 1/10 of the transient crater diameter, which equals to 0.84 times final crater rim-to-rim diameter for simple craters (Melosh, 1989). Therefore, we used this relationship for the diameter measured on the image to calculate the excavation depth of each of the simple craters located upon the mare unit. Note that most of the small craters less than 2 km in diameter are probably secondary craters thus they have smaller excavation depths than similar-sized primary craters (Oberbeck, 1975; McEwen & Bierhaus, 2006), indicating that the calculated excavation depths are the upper bound for the actual values.

The regolith constitutes the uppermost layer of the reconstructed stratigraphic column (A in Fig. 9), with a thickness of ~2.5 m to 7.5 m (the regolith in the northeastern part is thicker than in the southwestern part in the landing region Fig. 7). The main uncertainties in the regolith thickness estimates come from LROC NAC images with the necessary illumination geometry (incidence angle less than 55°), the determination of rim-to-rim diameter of craters, and the limitations of the estimation method (Quaide & Oberbeck, 1968).

Beneath the regolith is the Finsen LCP-bearing ejecta layer (B in Fig. 9) (which might be discontinuous or variable in thickness). Represented in blue tones in the MI color composite (Fig. 5d), this layer is excavated by craters ~66 to 336 m in diameter (Fig. 6a). The majority of these craters is 96 m to 156 m in diameter (Fig. 6a), suggesting that the LCP-bearing material is at least ~8 m to 13 m deep.

The HCP-bearing layer (D+E+F in Fig. 9) is exposed in the orange-toned ejecta in the MI color composite (Fig. 5d) of larger craters with diameters ranging from 268 m to 988 m (Fig. 6b) as well as *Ba Jie* crater. The majority of orange toned ejecta craters fall in the 388 m to 628 m range in diameter (Fig. 6b), indicating that the HCP-bearing materials (D) are at least ~33 m to 53 m deep. *Ba Jie* crater is ~3.7 km in diameter, suggesting that local minimal depth of the HCP-bearing materials (and hence mare unit) is greater than 310 m. The spectrum extracted from the site 5 of *Ba Jie* crater's ejecta have a deeper absorption band than the spectra of sites 6 and 7 (Fig. 5e). This absorption band depth difference could indicate that the material of site 5 is slightly distinct compared to material of sites 6 and 7, possibly more enriched in HCP or with a different grain size or texture (or less mature). Alternatively, the ejecta could be thicker at site 5 and less mixed with the underlying likely-space-weathered layer, resulting in a more intense signature. Spectral variations within the ejecta of *Ba Jie* crater (Fig. 5d and 5e) could hint at a subtle vertical compositional difference in the layer of HCP-bearing materials. The material located at site 5 (layer F) are from deeper portions of the pre-impact stratigraphy than the material located at sites 6 and 7, due to the fact that the deeper-seated material tends to be ejected closer to the crater rim (Stöffler, Gault, Wedekind, & Polkowski, 1975). Therefore, there is probably a layer of enriched HCP-bearing material (F) under the HCP-bearing-material layer, and could imply a possible paleo-regolith layer (E) between layers D and F if there were at least two episodes of basalt emplacement. The paleo-regolith thickness (if such a layer exists) could be studied with the radar instrument onboard the Chang'E-4 rover, similarly to the detections made at the Chang'E-3 landing site (Xiao et al., 2015). It appears reasonable to speculate that there could be somewhere in the stratigraphy a layer of mixed LCP and HCP-bearing material (C) due to collision of these two types of materials. However, we are not able to constrain the thickness of this mixed layer. The main uncertainties of the reconstructed stratigraphy come from ejecta of unidentified

impact craters, mixing of ejecta of local materials, and products of uncertain geological events between stratigraphic layers.

We propose a stratigraphic column with several layers beneath the HCP-bearing-material layer/ mare unit based on the regional setting and previous geological maps (Wilhelms et al., 1979; Yingst et al., 2017). However, the thickness of these layers cannot be constrained using available data and previous mapping results. We expect a layer G made of ejected material from Imbrian-aged craters (e.g., Alder) resurfacing HCP-bearing basalts. Layer B to G were formed during the Imbrian epoch. Ejecta of Leibnitz crater (H) occurred as the layer beneath, and this impact event occurred in Nectarian. Then there should be a layer (I) of breccia from Von Kármán crater forming event lying above the target materials (J) of Von Kármán crater. Layer I and J are of pre-Nectarian age (Fig. 9), likely to be part of the SPA basin Mg-Pyroxene Annulus (Moriarty and Pieters, 2018).

The two Ground Penetrating Radars onboard the CE-4 rover will be able to reveal the subsurface structure of the landing area and test the stratigraphy predicted in this study. In a manner similar to the CE-3 Yutu rover, the radar system of the CE-4 rover has two frequency channels with different penetrating depths and vertical resolutions: Channel 1 has a frequency of 40 -80 MHz whereas Channel 2 has a frequency of 250 - 750 MHz (Jia et al., 2018). The radar system on the Chang'E-3 mission demonstrated that the Channel 2 radar could detect details of the subsurface structures up to a depth of ~12 m, and the Channel 1 radar could reveal subsurface structures up to ~400 m (Xiao et al., 2015). Therefore, the Ground Penetrating Radars Channel 1 can detect layer A, B, C, D, E, F, and it could detect layer G, H, I, J depending on their thickness. Channel 2 could detect detailed structures within layers A, B, and the upper portion of the layer C.

4.4 The origin of the LCP bearing materials

The LCP bearing materials have relatively higher albedo compared to the relatively lower albedo mare basalts in the landing region. Regional geological context suggests that the LCP-bearing materials are part of the ejecta of the Finsen crater forming event (section 3.1). Besides Finsen crater, we have surveyed the nearby regions for younger craters that might have contributed ejecta over the landing region. Von Kármán L and Von Kármán L' adjacent to the landing region are the two large craters that are younger than the mare units, and they have inevitably launched ejecta into the landing region. We estimate the thickness of ejecta deposits formed by the impact of ejecta from Finsen, Von Kármán L and Von Kármán L' craters. First, we estimate the ejecta thickness distribution. Then, the thickness of local material excavated by the impact of ejecta is derived from empirical equation. Finally, the ejecta deposit thickness is the sum of ejecta from other craters and local material. Assuming a power law distribution of ejecta with slope of -3 (McGetchin et al., 1973) and using the scaling relationship between ejecta thickness at final crater rim crest and final crater radius given by Sharpton (2014), we estimate the ejecta thickness distribution by using this relationship $T = 3.95R^{0.399}\left(r/R\right)^{-3}$, where *r* is the distance from crater center in meters, and *R* is the final crater radius (all in meters). Therefore, the amount of ejecta contributed from Finsen (Fig. 10a, diameter D=73 km) is the largest among the three craters, followed by Von Kármán L (Fig. 10b, diameter D=29 km) and Von Kármán L' (Fig. 10c, diameter *D*=29 km). Assuming the incident angle of ejecta was 75°, Oberbeck et al. (1975) established an empirical model that can estimate the excavation efficiency (μ) of crater ejecta for given thickness of ejecta and the distance from crater center based on the analysis of Copernicus secondary craters (i.e., $\mu = 4.5\times10^{-5}r^{0.87}$, all in meters). However, recent works (e.g., Petro & Pieters, 2006; Xie & Zhu, 2016) suggested that the authors may have overestimated the excavation efficiency. Here, we adopt half of excavation efficiency of Oberbeck et al., (1975)

(i.e., $\mu = 2.25\times10^{-5} r^{0.87}$) according to the result of Petro & Pieters (2006). The thickness of local material excavated by the ejecta from either Von Kármán L or Von Kármán L' is predicted to be smaller than 1 m, whereas the thickness of Finsen ejecta is larger than 2.5 m (Fig. 10a). In addition, Finsen crater is older than both Von Kármán L and Von Kármán L' (Wilhelms et al., 1979; Yingst et al., 2017). Therefore, the ejecta from Von Kármán L or Von Kármán L' is expected to rework the ejecta deposits formed by Finsen crater ejecta. The thickness of ejecta deposits including the excavated local material and the total accumulated ejecta is predicted to vary from about 7.2-15.5 m (Fig. 10d), which is consistent with the depth of LCP bearing materials discussed previously. This is independent evidence that the LCP bearing materials were likely from Finsen crater, Von Kármán L and Von Kármán L'.

LCP bearing materials are pervasive across the SPA basin, including the central peak of Finsen Crater (Pieters et al., 2001; Moriarty, Pieters, & Isaacson, 2013; Moriarty and Pieters, 2018). However, the origin of the LCP bearing materials is still under debate. The LCP-bearing material could correspond to exposed KREEP-related Mg-suite rocks (Pieters, Tompkins, Head, & Hess, 1997; Klima et al., 2011) or the differentiated upper layer of the hypothesized SPA melt sheet (Nakamura et al., 2009; Uemoto et al., 2017). Alternatively, the LCP bearing materials could come from a LCP-dominated lunar upper mantle (Melosh et al., 2017; Moriarty and Pieters, 2018).

The hypotheses can be evaluated using geological context, but it is challenging to use orbital remote sensing data to pin down the origin of the LCP bearing materials due to lack of detailed geochemical data. The definitive way to establish the origin of the LCP bearing materials is by sample return (e.g. Jolliff et al., 2010), and the current payloads onboard the Chang'E-4 mission are not designed to reveal element distribution for surface materials. However, we point out that the penetrating radar onboard the CE-4 rover can test and help

verify the stratigraphy of the landing area, which might be used to indirectly infer the composition (e.g., by backward modelling for the dielectric constant) and provide additional clues about the origin of the LCP-bearing materials. These LCP-bearing materials could help to better constrain the history of the SPA region (Moriarty and Pieters, 2018) and might represent high priority targets for future sample return missions, e.g., Chang'E-6.

5 Conclusions

The Chinese CE-4 lunar mission will be the first in-situ exploration to explore the surface of the Moon and study its environment on the farside. The selected landing area is located in the southern portion of the Von Kármán crater, on the top of the infilling mare unit, and within the SPA basin (Fig. 1). We characterized the terrain and geological characteristics of the landing region using multi-source remote sensing datasets. The main conclusions are as follows:

1. The landing region (45°S - 46°S, 176.4°E - 178.8°E) is generally flat at a length scale of 59 m and located within a rather homogenous mare unit.
2. The absolute model age of the mare unit within Von Kármán crater is 3.6 Ga (+.09, -.2), based on multiple crater size-frequency distribution measurements.
3. Secondary craters have almost covered the entire landing area. The oldest secondary craters (NE-SW direction) look degraded and converge to Finsen crater. N-S direction secondary craters are superposing on them, and they are converging to Antoniadi crater. The youngest secondary craters are NE-SW, and they are likely from Von Kármán L and Von Kármán L'.
4. The thickness of the regolith is estimated to be ~2.5 m to 7.5 m in the landing area.
5. Extensive sinuous ridges and sinuous troughs are identified in the landing area. They are related to *Ba Jie* crater spatially, but the origin is controversial. The ground

penetrating radar onboard CE-4 rover will reveal the subsurface structure and provide clues to the origin of these linear features.

6. Spectral variations among the ejecta of craters of various sizes reveal the subsurface structures. Along with the estimated thickness of the regolith, crater size-frequency distribution absolute model age and previously geological mapping results, we proposed a stratigraphic profile of the landing area that can be tested with CE-4 ground penetrating radar data.
7. LCP-bearing material, probably excavated from the nearby Finsen Crater from a depth < 7 km, are widespread in the landing region and could bring more clues about SPA history.
8. The detailed stratigraphy and the diversity of farside geologic units sampled by impact craters in the region (both in the vertical and lateral sense) and delivered to the landing and traverse area to form secondary craters, ensure that the Von Kármán landing site will be an excellent candidate for the first sample return mission to the lunar farside by Chang'E-6. Soils in the Von Kármán regolith are very likely to contain samples of farside lunar maria, a diversity of farside highland rock types, and samples of the SPA basin Mg-Rich Annulus (impact melt and possible mantle of the SPA basin). The Change'E-4 mission and surface traverses will provide the surface and three-dimensional stratigraphic information necessary to help refine the lateral and vertical stratigraphy to ensure optimal sample return.

Acknowledgments

Reviews by Daniel Moriarty, Aileen Yingst and an anonymous reviewer were incredibly helpful to help clarify the paper, and much appreciated. We thank the editor Steven A. Hauck II for comments and editorial help. LRO NAC and WAC data, Chandrayaan-1 M^3 data were downloaded from the PDS (https://pds.nasa.gov/). MI and TC data were downloaded from the SELENE archive (http://darts.isas.jaxa.jp/planet/pdap/selene/). The data of regolith estimation, subsurface reconstruction and crater count are available in the supplementary materials. J. H. was supported by National Scientific Foundation of China (No. 41773061), the Fundamental Research Funds for the Central Universities, China University of Geosciences (Wuhan) (No. CUGL160402 and No. CUG2017G02). Z.X. was supported by National Scientific Foundation of China (No. 41773063). The work of J. F. is supported by the CNES (Luna/ExoMars APR). The work of M. M. was supported by a Netherlands Organization for Scientific Research (NWO) grant. The authors also thank Dr. Qiong Wang for the discussion of the landing region.

References

Atwood-Stone, C., Bray, V. J., & McEwen, A. S. (2016). A new study of crater concentric ridges on the Moon. *Icarus, 273*, 196-204. doi: https://doi.org/10.1016/j.icarus.2016.03.012

Barker, M., Mazarico, E., Neumann, G., Zuber, M., Haruyama, J., & Smith, D. (2016). A new lunar digital elevation model from the Lunar Orbiter Laser Altimeter and SELENE Terrain Camera. *Icarus, 273*, 346-355.

Bart, G. D., R. D. Nickerson, M. T. Lawder & H. Melosh (2011) Global survey of lunar regolith depths from LROC images. Icarus, 215, 485-490

Bart, G. D. (2014). The quantitative relationship between small impact crater morphology and regolith depth. Icarus, 235, 130-135.

Besse, S., Sunshine, J., Staid, M., Boardman, J., Pieters, C., Guasqui, P., . . . Li, J.-Y. (2013). A visible and near-infrared photometric correction for Moon Mineralogy Mapper (M^3). *Icarus, 222*(1), 229-242.

Binder, A. B. (1982). Post-Imbrian global lunar tectonism: Evidence for an initially totally molten Moon. *The Moon and the Planets, 26*(2), 117-133.

Boardman, J. W., Pieters, C., Green, R., Lundeen, S., Varanasi, P., Nettles, J., . . . Taylor, L. (2011). Measuring moonlight: An overview of the spatial properties, lunar coverage, selenolocation, and related Level 1B products of the Moon Mineralogy Mapper. *Journal of Geophysical Research: Planets, 116*(E6).

Clark, R. N., Pieters, C. M., Green, R. O., Boardman, J., & Petro, N. E. (2011). Thermal removal from near‐infrared imaging spectroscopy data of the Moon. *Journal of Geophysical Research: Planets, 116*(E6).

National Research Council. (2007). *The scientific context for exploration of the Moon*: National Academies Press.

Fa, W., Liu, T., Zhu, M. H., & Haruyama, J. (2014). Regolith thickness over Sinus Iridum: Results from morphology and size‐frequency distribution of small impact craters. *Journal of Geophysical Research: Planets, 119*(8), 1914-1935.

Fang, G.-Y., Zhou, B., Ji, Y.-C., Zhang, Q.-Y., Shen, S.-X., Li, Y.-X., . . . Lu, W. (2014). Lunar Penetrating Radar onboard the Chang'e-3 mission. *Research in astronomy and astrophysics, 14*(12), 1607.

Garrick-Bethell, I., & Zuber, M. T. (2009). Elliptical structure of the lunar South Pole-Aitken basin. *Icarus, 204*(2), 399-408.

Green R, Pieters C, Mouroulis P, Eastwood M, Boardman J, Glavich T, Isaacson P, Annadurai M, Besse S, and Barr D. (2011) The Moon Mineralogy Mapper (M3) imaging spectrometer for lunar science: Instrument description, calibration, on‐orbit measurements, science data calibration and on‐orbit validation. Journal of Geophysical Research: Planets, 116.

Haruyama, J., Ohtake, M., Matsunaga, T., Morota, T., Honda, C., Yokota, Y., . . . Josset, J. L. (2009). Long-lived volcanism on the lunar farside revealed by SELENE Terrain Camera. *Science, 323*(5916), 905-908. doi: 10.1126/science.1163382

Hawke, B. R., Blewett, D. T., Lucey, P. G., Smith, G. A., Bell, J. F., Campbell, B. A., & Robinson, M. S. (2004). The origin of lunar crater rays. *Icarus, 170*(1), 1-16. doi: 10.1016/j.icarus.2004.02.013

He, Z.-P., Wang, B.-Y., Lü, G., Li, C.-L., Yuan, L.-Y., Xu, R., . . . Wang, J.-Y. (2014). Operating principles and detection characteristics of the Visible and Near-Infrared Imaging Spectrometer in the Chang'e-3. *Research in astronomy and astrophysics, 14*(12), 1567.

Head, J. W., Murchie, S., Mustard, J. F., Pieters, C. M., Neukum, G., McEwen, A., . . . Belton, M. J. (1993). Lunar impact basins: New data for the western limb and far side

(Orientale and South Pole‐Aitken basins) from the first Galileo flyby. *Journal of Geophysical Research: Planets, 98*(E9), 17149-17181.

Huang, J., Xiao, L., He, X., Qiao, L., Zhao, J., & Li, H. (2011). Geological characteristics and model ages of Marius Hills on the Moon. *Journal of Earth Science, 22*(5), 601-609. doi: 10.1007/s12583-011-0211-8

Jia, Y. Z., Zou, Y. L., Xue, C. B., Ping, J. S., Yan, J., & Ning, Y. M. (2018). Scientific Objectives and Payloads of Chang'E-4 Missionormalsize (in Chinese). *Chinese Journal of Space Science, 38*(1), 118-130.

Jolliff, B. L., Shearer, C. K., Papanastassiou, D. A., Alkalai, L., & Team, M. (2010, September). MOONRISE: South Pole-Aitken Basin sample return mission for solar system science. In Annual Meeting of the Lunar Exploration Analysis Group (Vol. 1595, p. 31).

Kato, M., Sasaki, S., & Takizawa, Y. (2010). The Kaguya mission overview. *Space Science Reviews, 154*(1-4), 3-19.

Klima, R. L., Pieters, C. M., Boardman, J. W., Green, R. O., Head, J. W., Isaacson, P. J., . . . Tompkins, S. (2011). New insights into lunar petrology: Distribution and composition of prominent low-Ca pyroxene exposures as observed by the Moon Mineralogy Mapper (M^3). *Journal of Geophysical Research: Planets, 116*(E6), n/a-n/a. doi: 10.1029/2010JE003719

Ling, Z., Jolliff, B. L., Wang, A., Li, C., Liu, J., Zhang, J., . . . Xiao, L. (2015). Correlated compositional and mineralogical investigations at the Chang′ e-3 landing site. *Nat Commun, 6*, ncomms9880.

Losiak, A., Wilhelms, D., Byrne, C., Thaisen, K., Weider, S., Kohout, T., . . . Kring, D. (2009). *A new lunar impact crater database.* Paper presented at the Lunar and Planetary Science Conference.

Lucchitta, B. K. (1977). Crater clusters and light mantle at the Apollo 17 site; a result of secondary impact from Tycho. *Icarus, 30*(1), 80-96.

Martinot, M., Besse, S., Flahaut, J., Quantin‐Nataf, C., Lozac'h, L., & Westrenen, W. v. (2018). Mineralogical diversity and geology of Humboldt crater derived using Moon Mineralogy Mapper data. *Journal of Geophysical Research: Planets*.

McEwen, A. S., & Bierhaus, E. B. (2006). The importance of secondary cratering to age constraints on planetary surfaces. *Annu. Rev. Earth Planet. Sci., 34*, 535-567.

McGetchin, T. R., M. Settle, and J. Head (1973), Radial thickness variation in impact crater ejecta: Implications for lunar basin deposits, *Earth And Planetary Science Letters, 20*(2), 226–236.

Melosh, H. J. (1989). Impact cratering: A geologic process. *Research supported by NASA. New York, Oxford University Press (Oxford Monographs on Geology and Geophysics, No. 11), 1989, 253 p., 11*.

Melosh, H. J., Kendall, J., Horgan, B., Johnson, B., Bowling, T., Lucey, P., & Taylor, G. (2017). South Pole–Aitken basin ejecta reveal the Moon's upper mantle. *Geology, 45*(12), 1063-1066.

Michael, G. G., Kneissl, T., & Neesemann, A. (2016). Planetary surface dating from crater size-frequency distribution measurements: Poisson timing analysis. *Icarus, 277*, 279-285.

Michael, G. G., & Neukum, G. (2010). Planetary surface dating from crater size–frequency distribution measurements: Partial resurfacing events and statistical age uncertainty. *Earth and Planetary Science Letters, 294*(3-4), 223-229. doi: 10.1016/j.epsl.2009.12.041

Moriarty, D. P., Pieters, C. M., & Isaacson, P. J. (2013). Compositional heterogeneity of central peaks within the South Pole-Aitken Basin. *Journal of Geophysical Research:*

Planets, *118*(11), 2310-2322. doi: 10.1002/2013JE004376

Moriarty, D. P., and C. M. Pieters (2018) The Character of South Pole - Aitken Basin: Patterns of Surface and Sub-Surface Composition, Journal of Geophysical Research: Planets, n/a-n/a, doi:10.1002/2017JE005364.

Morrison, D. A. (1998). Did a thick South Pole-Aitken Basin melt sheet differentiate to form cumulates? Lunar and Planetary Science Conference (Vol. 29).

Nakamura, R., Matsunaga, T., Ogawa, Y., Yamamoto, S., Hiroi, T., Saiki, K., . . . Yokota, Y. (2009). Ultramafic impact melt sheet beneath the South Pole–Aitken basin on the Moon. *Geophysical Research Letters*, *36*(22), n/a-n/a. doi: 10.1029/2009GL040765

Neukum, G., Ivanov, B. A., & Hartmann, W. K. (2001). Cratering Records in the Inner Solar System in Relation to the Lunar Reference System. *12*, 55-86. doi: 10.1007/978-94-017-1035-0_3

Oberbeck, V. R., & Quaide, W. L. (1967). Estimated thickness of a fragmental surface layer of Oceanus Procellarum. Journal of Geophysical Research, 72(18), 4697-4704.

Oberbeck, V. R. (1975). The role of ballistic erosion and sedimentation in lunar stratigraphy. *Reviews of Geophysics*, *13*(2), 337-362.

Oberbeck, V. R., Hörz, F., Morrison, R., Quaide, W., & Gault, D. (1975). On the origin of the lunar smooth-plains. *The Moon*, *12*(1), 19–54.

Ohtake, M., Haruyama, J., Matsunaga, T., Yokota, Y., Morota, T., & Honda, C. (2008). Performance and scientific objectives of the SELENE (KAGUYA) Multiband Imager. *Earth, planets and space*, *60*(4), 257-264.

Ohtake, M., Uemoto, K., Yokota, Y., Morota, T., Yamamoto, S., Nakamura, R., . . . Ishihara, Y. (2014). Geologic structure generated by large‐impact basin formation observed at the South Pole‐Aitken basin on the Moon. Geophysical Research Letters, 41(8), 2738-2745.

Pasckert, J. H., Hiesinger, H., & van der Bogert, C. H. (2018). Lunar farside volcanism in and around the South Pole–Aitken basin. *Icarus, 299,* 538-562.

Petro, N. E., & Pieters, C. M. (2006). Modeling the provenance of the Apollo 16 regolith. *Journal of Geophysical Research: Planets, 111*(E9). doi: 10.1029/2005je002559

Pieters, C. M., Head, J., Sunshine, J., Fischer, E., Murchie, S., Belton, M., . . . Neukum, G. (1993). Crustal diversity of the Moon: Compositional analyses of Galileo solid state imaging data. *Journal of Geophysical Research: Planets, 98*(E9), 17127-17148.

Pieters, C. M., Tompkins, S., Head, J. W., & Hess, P. C. (1997). Mineralogy of the Mafic Anomaly in the South Pole-Aitken Basin: Implications for excavation of the lunar mantle. *Geophysical Research Letters, 24*(15), 1903-1906. doi: 10.1029/97GL01718

Pieters, C., Head, J., Gaddis, L., Jolliff, B., & Duke, M. (2001). Rock types of South Pole‐Aitken basin and extent of basaltic volcanism. Journal of Geophysical Research: Planets, 106(E11), 28001-28022.

Pieters, C. M., Boardman, J., Buratti, B., Chatterjee, A., Clark, R., Glavich, T., . . . Malaret, E. (2009). The Moon Mineralogy Mapper (M^3) on Chandrayaan-1. *Current Science,* 500-505.

Potter, R. W. K., Collins, G. S., Kiefer, W. S., McGovern, P. J., & Kring, D. A. (2012). Constraining the size of the South Pole-Aitken basin impact. *Icarus, 220*(2), 730-743. doi: 10.1016/j.icarus.2012.05.032

Quaide, W. L., & Oberbeck, V. R. (1968). Thickness determinations of the lunar surface layer from lunar impact craters. *Journal of Geophysical Research, 73*(16), 5247-5270.

Robinson, M. S., Brylow, S. M., Tschimmel, M., Humm, D., Lawrence, S. J., Thomas, P. C., . . . Hiesinger, H. (2010). Lunar Reconnaissance Orbiter Camera (LROC) Instrument Overview. *Space Science Reviews, 150*(1-4), 81-124. doi: 10.1007/s11214-010-9634-2

Sharpton, V. L. (2014). Outcrops on lunar crater rims: Implications for rim construction mechanisms, ejecta volumes and excavation depths. *Journal of Geophysical Research: Planets, 119*(1), 154–168.

Smith, D. E., Zuber, M. T., Neumann, G. A., Lemoine, F. G., Mazarico, E., Torrence, M. H., . . . Duxbury, T. H. (2010). Initial observations from the lunar orbiter laser altimeter (LOLA). *Geophysical Research Letters, 37*(18).

Soderblom, L. A. (1970) A model for small‐impact erosion applied to the lunar surface. Journal of Geophysical Research, 75, 2655-2661.

Spudis, P. D., Gillis, J. J., & Reisse, R. A. (1994). Ancient multiring basins on the Moon revealed by Clementine laser altimetry. *Science*, *266*(5192), 1848-1851.

Stöffler, D., Gault, D., Wedekind, J., & Polkowski, G. (1975). Experimental hypervelocity impact into quartz sand: Distribution and shock metamorphism of ejecta. *Journal of Geophysical Research*, *80*(29), 4062-4077.

Staid, M. I., Pieters, C. M., Besse, S., Boardman, J., Dhingra, D., Green, R., . . . Kramer, G. (2011). The mineralogy of late stage lunar volcanism as observed by the Moon Mineralogy Mapper on Chandrayaan‐1. *Journal of Geophysical Research: Planets, 116*(E6).

Stuart-Alexander, D. E. (1978). *Geologic map of the central far side of the Moon*: US Geological Survey Washington, DC.

Uemoto, K., Ohtake, M., Haruyama, J., Matsunaga, T., Yamamoto, S., Nakamura, R., . . . Iwata, T. (2017). Evidence of impact melt sheet differentiation of the lunar South Pole-Aitken basin. *Journal of Geophysical Research: Planets, 122*(8), 1672-1686. doi: 10.1002/2016JE005209

Vaughan, W. M., & Head, J. W. (2014). Impact melt differentiation in the South Pole-Aitken basin: Some observations and speculations. *Planetary and Space Science, 91*, 101-106.

Weitz, C. M., & Head, J. W. (1999). Spectral properties of the Marius Hills volcanic complex and implications for the formation of lunar domes and cones. Journal of Geophysical Research-Planets, 104(E8), 18933-18956.

Wilhelms, D. E., Howard, K. A., & Wilshire, H. G. (1979). *Geologic map of the south side of the Moon*.

Wilhelms, D. E., John, F., & Trask, N. J. (1987). The geologic history of the Moon.

Wu, W. R., Wang, Q., Tang, Y. H., Yu, G. B., Liu, J. Z., Zhang, W., . . . Lu, L. L. (2017). Design of Chang'E-4 lunar farside soft-landing mission (in Chinese). *Journal of Deep Space Exploration, 4*(2), 111-117.

Xiao, Z. (2016), Size-frequency distribution of different secondary crater populations: 1. Equilibrium caused by secondary impacts, J. Geophys. Res. Planets, 121, 2404–2425, doi:10.1002/2016JE005139.

Xiao, L., Zhu, P., Fang, G., Xiao, Z., Zou, Y., Zhao, J., . . . Gao, Y. (2015). A young multilayered terrane of the northern Mare Imbrium revealed by Chang'E-3 mission. *Science, 347*(6227), 1226-1229. doi: 10.1126/science.1259866

Xie, M., & Zhu, M.-H. (2016). Estimates of primary ejecta and local material for the Orientale basin: Implications for the formation and ballistic sedimentation of multi-ring basins. *Earth and Planetary Science Letters, 440*, 71-80.

Yingst, R. A., & Head, J. W. (1997). Volumes of lunar lava ponds in South Pole‐Aitken and Orientale basins: Implications for eruption conditions, transport mechanisms, and magma source regions. *Journal of Geophysical Research: Planets*, *102*(E5), 10909-10931.

Yingst, R. A., & Head, J. W. (1999). Geology of mare deposits in South Pole‐Aitken basin as seen by Clementine UV/VIS data. *Journal of Geophysical Research: Planets, 104*(E8), 18957-18979.

Yingst, R., Chuang, F., Berman, D., & Mest, S. (2017). *Geologic Mapping of the Planck Quadrangle of the Moon (LQ-29).* Paper presented at the Lunar and Planetary Science Conference.

Zhang, H., Yang, Y., Yuan, Y., Jin, W., Lucey, P. G., Zhu, M. H., . . . Wan, W. (2015). In situ optical measurements of Chang'E‐3 landing site in Mare Imbrium: 1. Mineral abundances inferred from spectral reflectance. *Geophysical Research Letters*, *42*(17), 6945-6950.

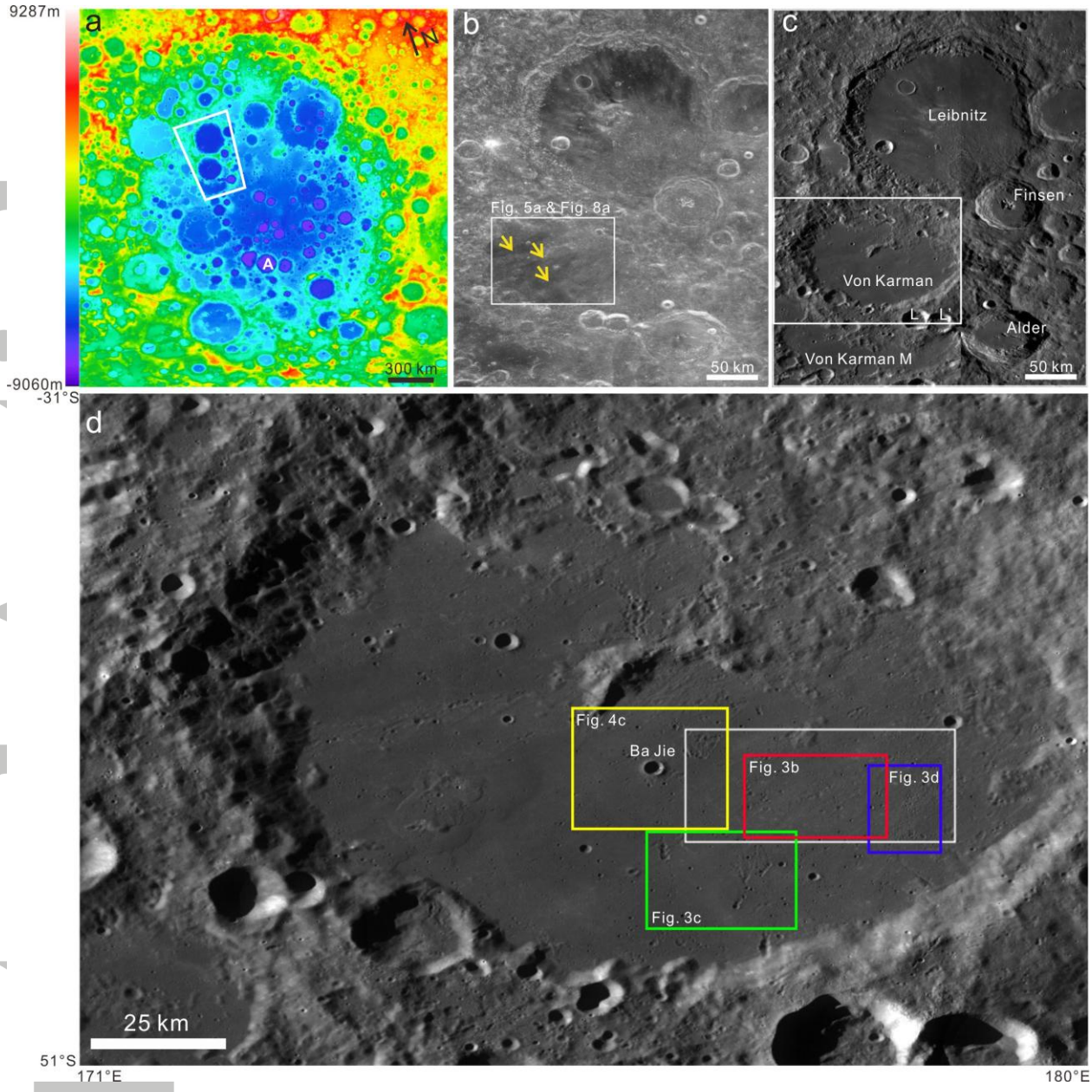

Fig. 1 a) Color-coded Lunar Orbiter Laser Altimeter (LOLA) Digital Elevation Model (DEM) of the South Pole-Aitken Basin (altitude scale on the left). The polygon shows the location of subsets b and c. Letter "A" indicates the location of the Antoniadi crater. b) Global normalized reflectance (incidence=30, emission=0, phase=30) of the 643 nm Lunar Reconnaissance Orbiter Camera (LROC) Wide-Angle Camera (WAC) mosaic of the Von Kármán area. The rectangle shows the location of Fig. 5a and Fig. 8a. Yellow arrows indicate the ray materials on the floor of Von Kármán crater and they are converged to Finsen crater. c) LROC WAC mosaic of the same area. The white box shows the location of subset d. d)

LRO WAC mosaic of Von Kármán crater. The white box shows the selected landing region, which shows the locations of Fig. 2a, Fig. 2b, red box in Fig. 3a, black boxes in Fig. 5c, Fig. 5d, Fig. 7, Fig. 9a, Fig. 9b, Fig. 9c and Fig. 9d. The red, green, blue and yellow rectangles show the locations of Fig. 3b, Fig. 3c, Fig. 3d and Fig. 4c, respectively. We informally named the unnamed impact crater (diameter D=3.6 km; central coordinates as 43.3°S 176.1°E) near the landing region as *Ba Jie*, which we use in italics to indicate its informal designation. North is towards the top in subsets b, c and d.

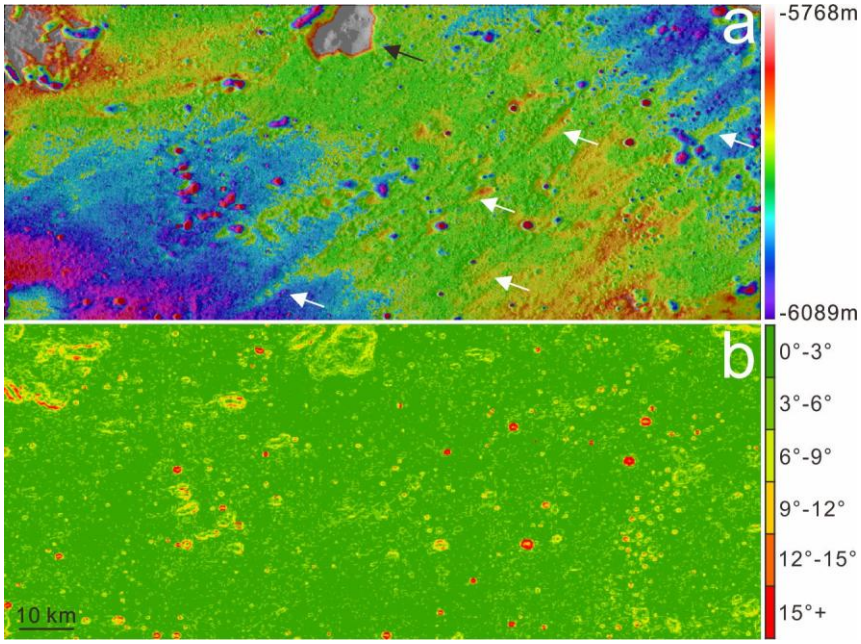

Fig. 2 a) Colorized SLDEM topography overlain in transparency over the TC morning mosaic of the landing region. The black arrow points to the mound with the highest altitude in this region. White arrows indicate NE-SW linear features with elevated topography. b) Slope map of the landing region calculated with a baseline of 59 m. The location of (a) and (b) is indicated in Fig. 1d.

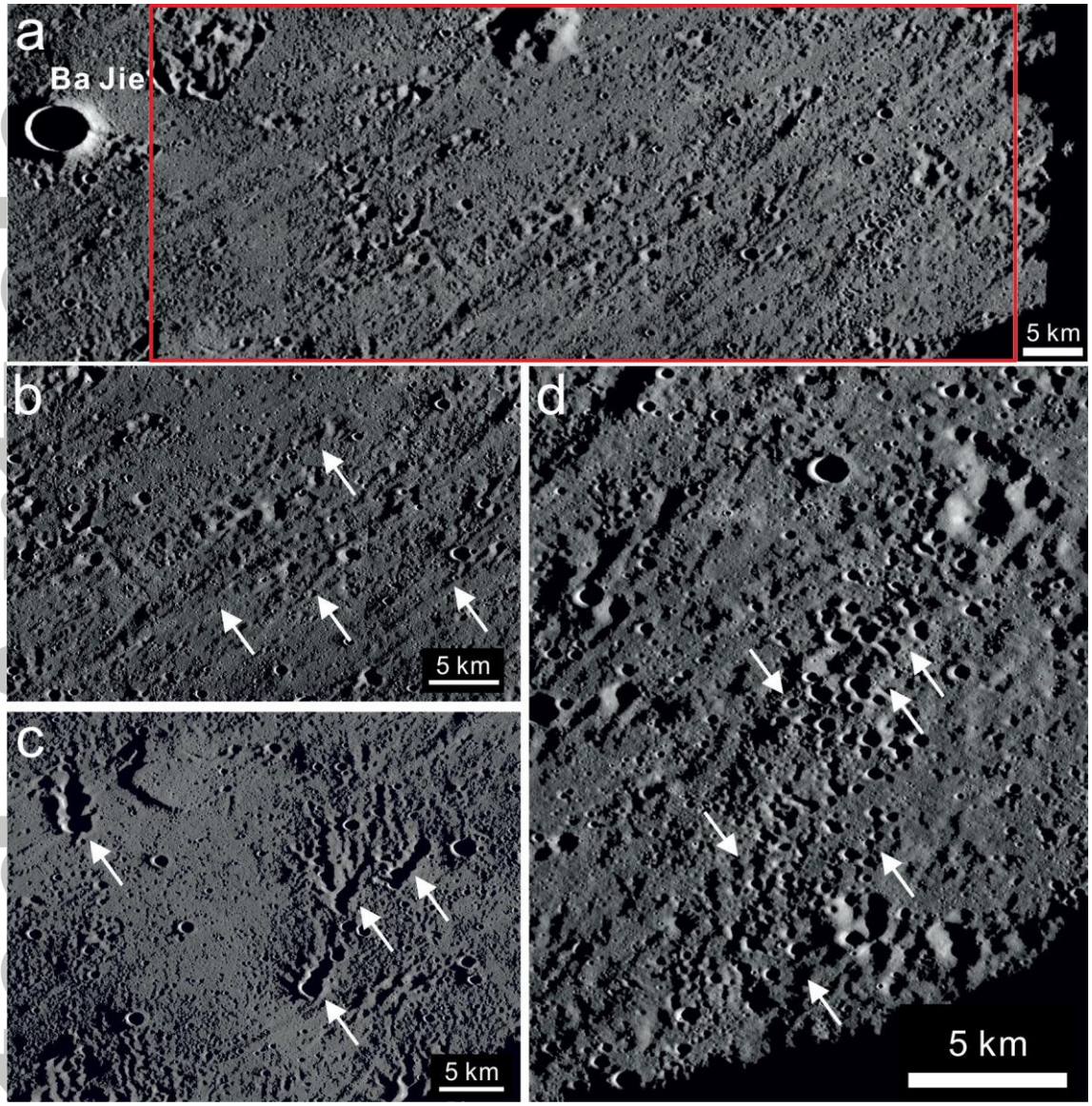

Fig. 3 a) TC Morning mosaic shows secondary craters occurrence all over the landing region (indicated by the red box). The red box is the same location of the white box in Fig. 1d. b) NE–SW trending linear features formed by Finsen, which are interpreted as highly degraded secondary craters with diameters > 500 m. c) N–S trending secondary craters (D>1 km) overlapping the previous NE–SW trending linear features formed by Finsen. The source crater is most likely Antoniadi crater. d) NE–SW relatively fresh secondary craters superposing the NE–SW trending linear features. The source craters are most likely the Von Kármán L and Von Kármán L' craters. North is up in all the panels. The locations of (b), (c), (d) are indicated in Fig. 1d.

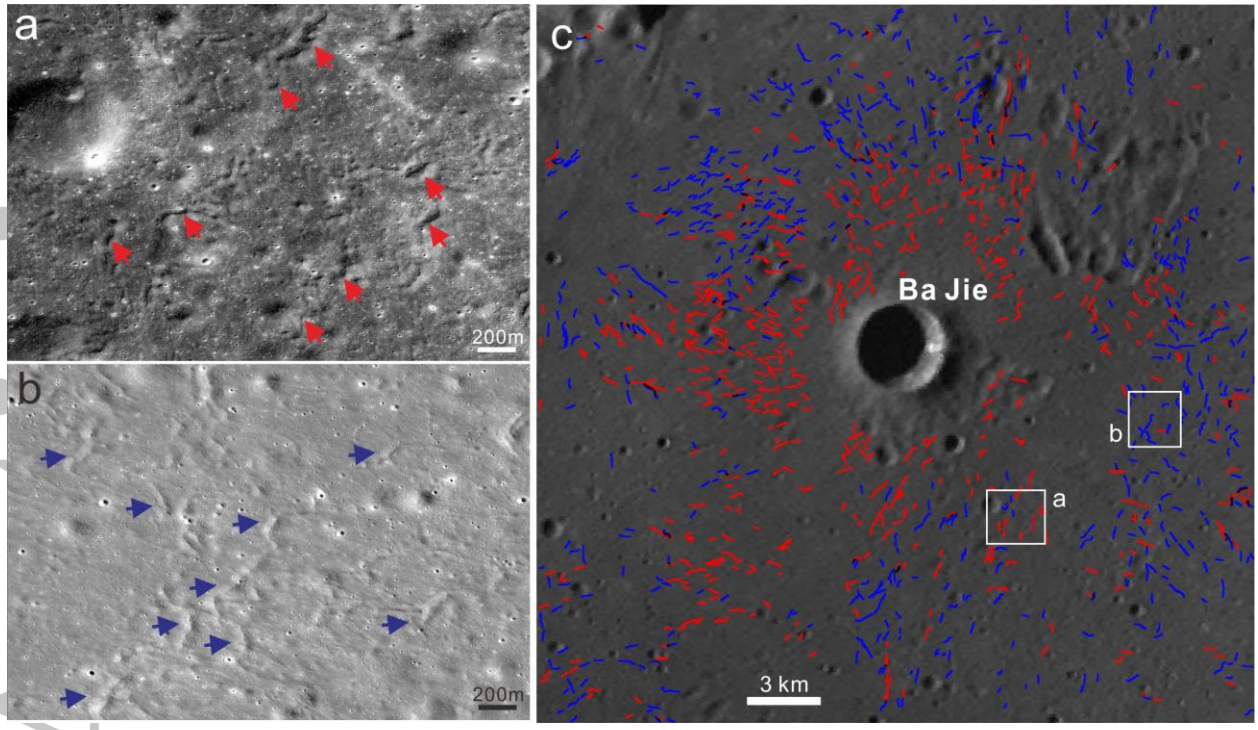

Fig. 4 a) LRO NAC image (M1100060445RE) of a region west of the landing region. Red arrows indicate the position of asymmetric sinuous ridges. b) LRO NAC image (M1183658592RE) of an area in the western part of the landing region. Blue arrows indicate the position of sinuous troughs. c) The spatial relationships between sinuous ridges and sinuous troughs observed in the vicinity *Ba Jie* crater. Red lines indicate sinuous ridges and blue lines indicate sinuous troughs. North is towards the top in all the panels.

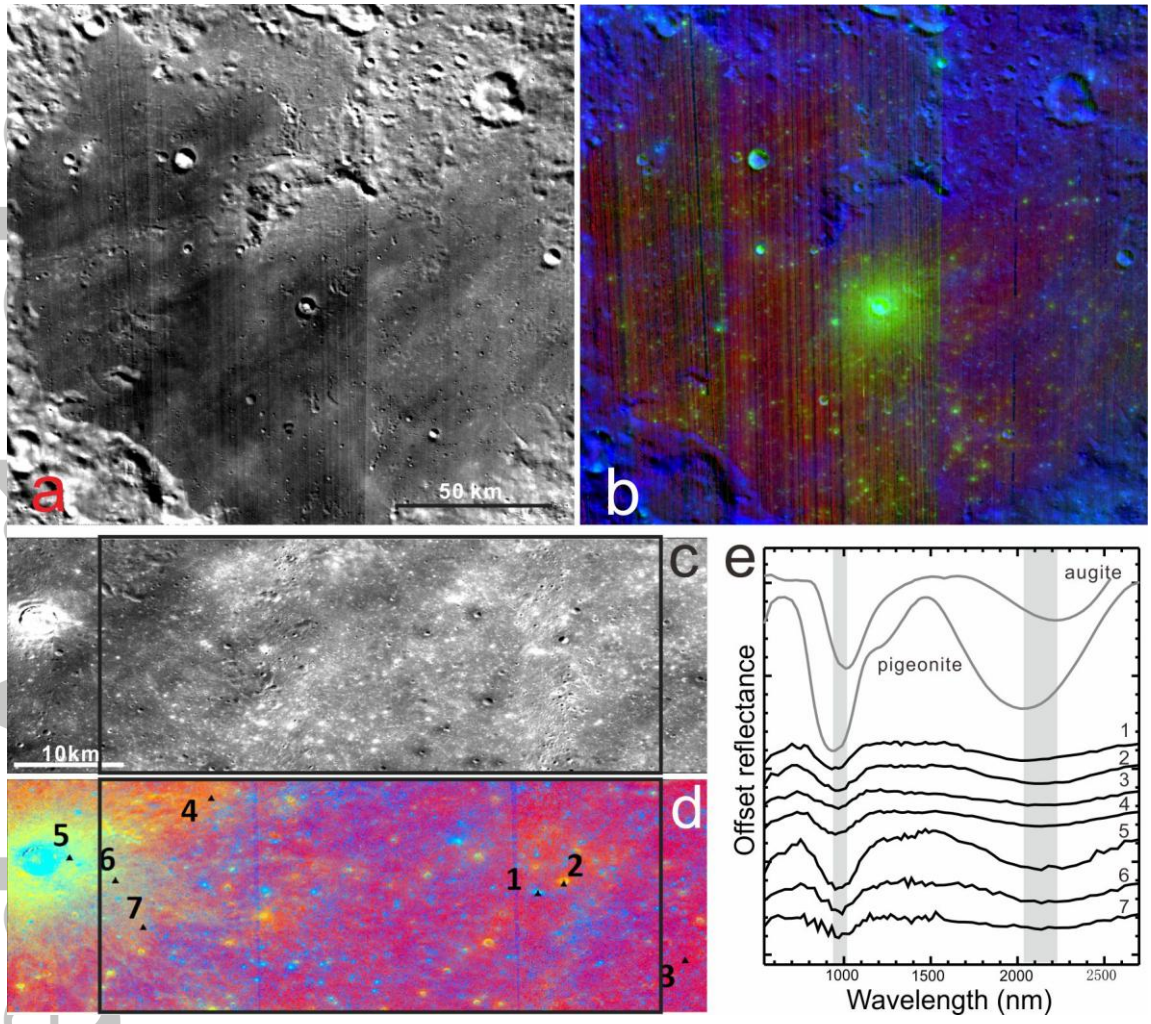

Fig.5 a) M³ 750 nm reflectance mosaic of Von Kármán crater (stretch: 0.044-0.082). High albedo linear features oriented WSW-ENE are visible on the crater floor, and they can be traced back to Finsen crater in Fig. 1b. The location of this subset and (b) is indicated in Fig. 1b. b) M³ color composite of Von Kármán crater (same region as a). R = 2 micron band center (2000-2500); G = 2 micron band depth (0.04-0.17); B = reflectance at 1580 nm (0.085-0.15). Stretch values are indicated in brackets. LCP-bearing material appears in light blue, and HCP-bearing material appears green. Spectral parameters were calculated using the method described in Martinot et al., (2018). c) MI 750 nm reflectance mosaic of the landing area. Relatively high albedo features are mostly associated with ejecta deposits of small fresh craters, and impact rays from the Finsen crater, whereas low albedo features are mostly associated with mare basalts and ejecta deposits of large craters. The landing area is indicated

as a black rectangle, which is indicated in Fig. 1d. d) RGB composite of MI data. R: 750 nm/415 nm (1.797-1.925), G: 950 nm/750 nm (0.877-1.034), B: 415 nm/750 nm (0.515-0.564). Stretch values are indicated in brackets. The landing area is indicated as a black rectangle, which is indicated in Fig. 1d. e) Continuum-removed M^3 spectra of locations (1 to 7) in Fig. 5d. Each spectrum corresponds to a single pixel. Spectra were processed with the method described in Martinot et al., (2018). A pigeonite (LCP) and an augite (HCP) spectrum from the RELAB database are displayed above the observed spectra for comparison (respective RELAB-ID: DL-CMP-008 and AG-TJM-010). Shaded areas represent the diversity of values of the 1 and 2 micron bands.

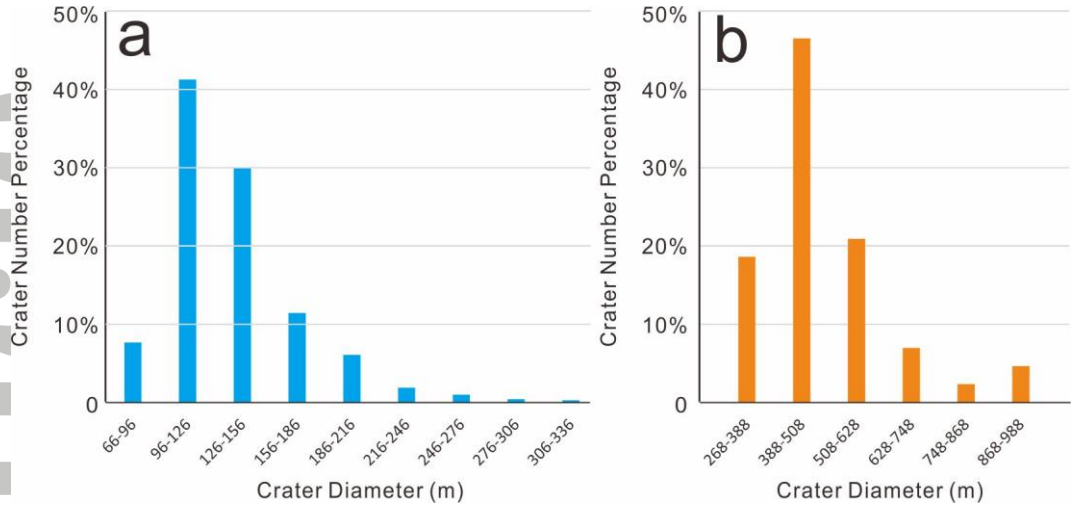

Fig.6 Diameter distribution of craters with a) low-Ca pyroxene bearing ejecta (blue) and b) high-Ca pyroxene bearing ejecta (orange) within the landing region (see Fig. 5d).

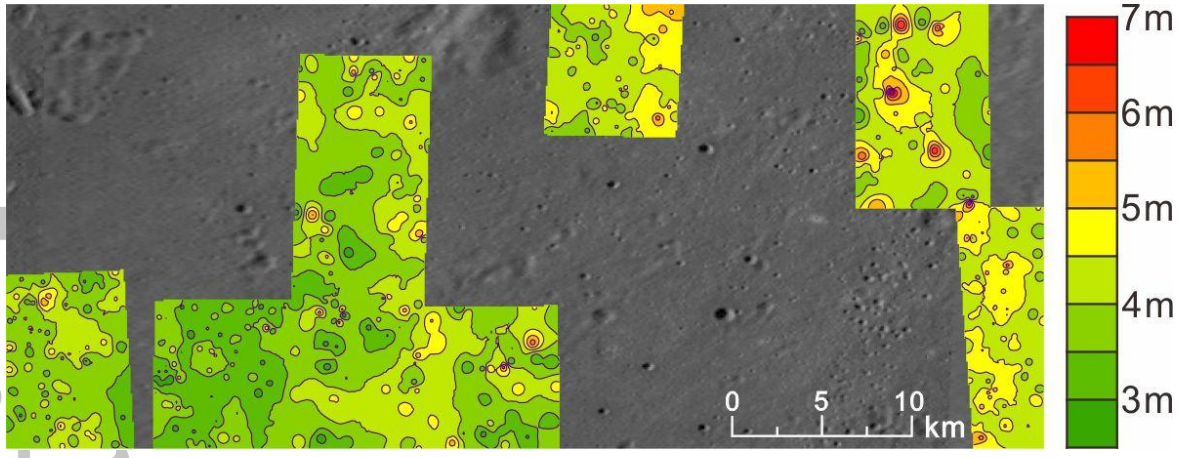

Fig.7 Estimated thickness contour of regolith in the landing region based on available LROC NAC images with incidence angle inferior to 55°. The background image is WAC mosaic, and the location is indicated in Fig. 1d. The IDs of NAC images used are M143453659RE, M143453659LE, M143460468RE, M143460468LE, M156434145RE, M156434145LE, M189435642RE, M189435642LE, M1133052548RE, M1133052548LE, M1145979809RE, M1145979809LE, M1163658519LE.

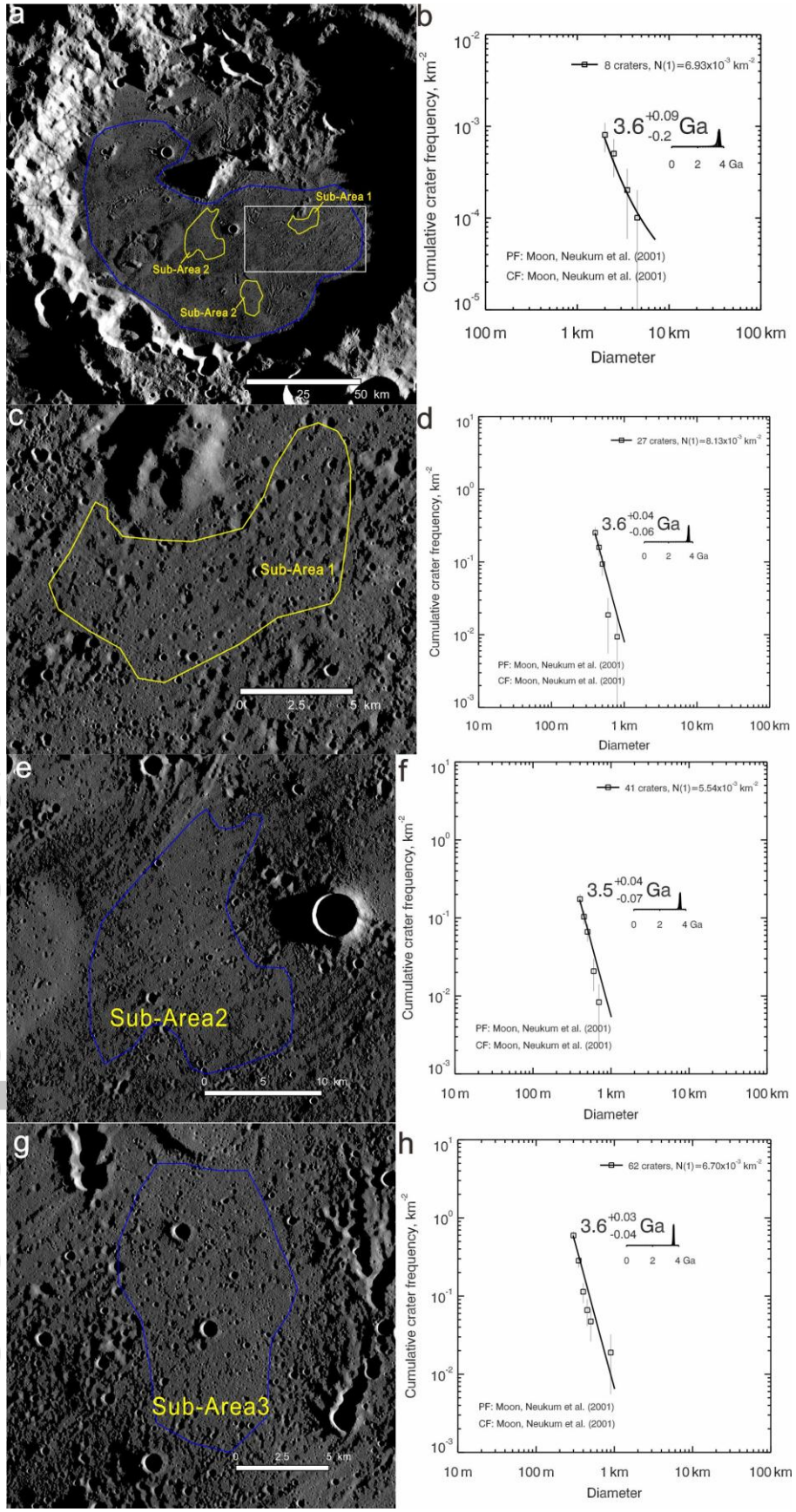

Fig.8. Absolute model ages derived from crater statistics for the mare unit located within the floor of Von Kármán crater. (a) Counting areas on the crater floor based on Kaguya TC mosaic. The mare units on the crater floor were classified as a single geological unit based on recent geological mapping (Yingst et al., 2017). The blue area shows the counting area where only craters larger than 2 km in diameter are used in deriving the model age. The locations of the three sub-areas are shown in yellow polygons. These regions were selected as they are less affected by obvious secondaries in comparison to the rest of the crater floor. b) Model age for the mare unit derived from probability analysis (Michael et al., 2016). c) Detailed surface morphology of the sub-area 1 shown in Kaguya TC mosaic. This area is located within the selected landing area, where the population of obvious secondary craters is smaller. Degraded secondary craters within this sub-area are less than 400 m in diameter. (d) Model age for the sub-area 1 on the mare surface derived from probability analysis (Michael et al., 2016). (e) Context of sub-area 2 shown by Kaguya TC mosaic and the location of the counting area (blue polygon). (f) Model ages derived for the crater population in sub-area 2. (g) Context of sub-area 3 shown by Kaguya TC mosaic and the counting area (blue polygon). (h) Model ages derived for the crater population in sub-area 3. North is to the top in (a), (c), (e) and (g).

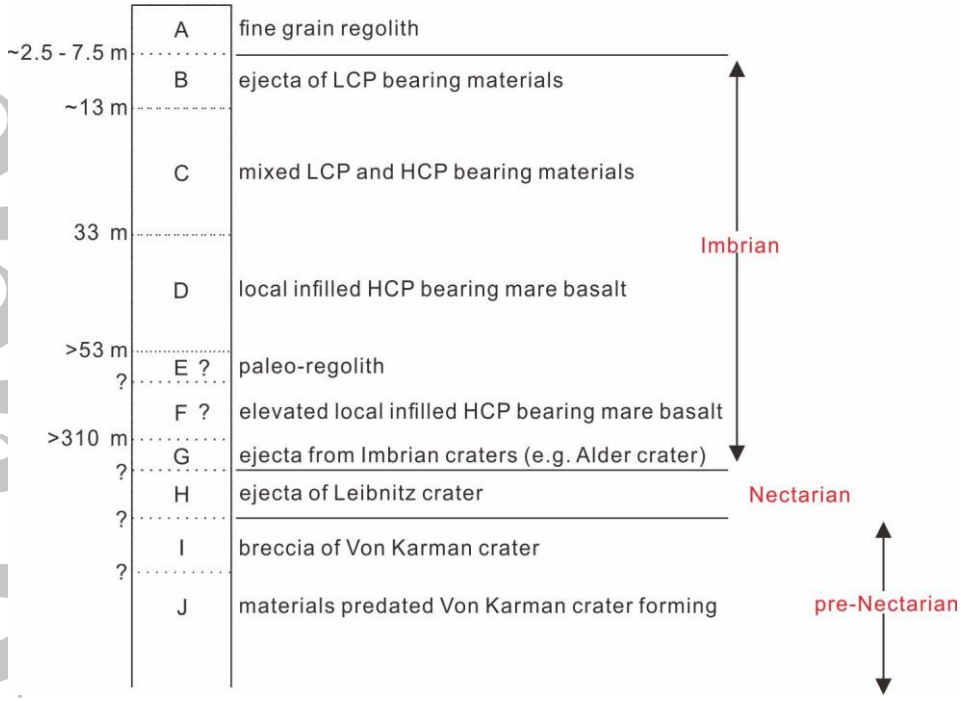

Fig. 9 Proposed stratigraphy of the landing region. The thickness of the layers is not to scale

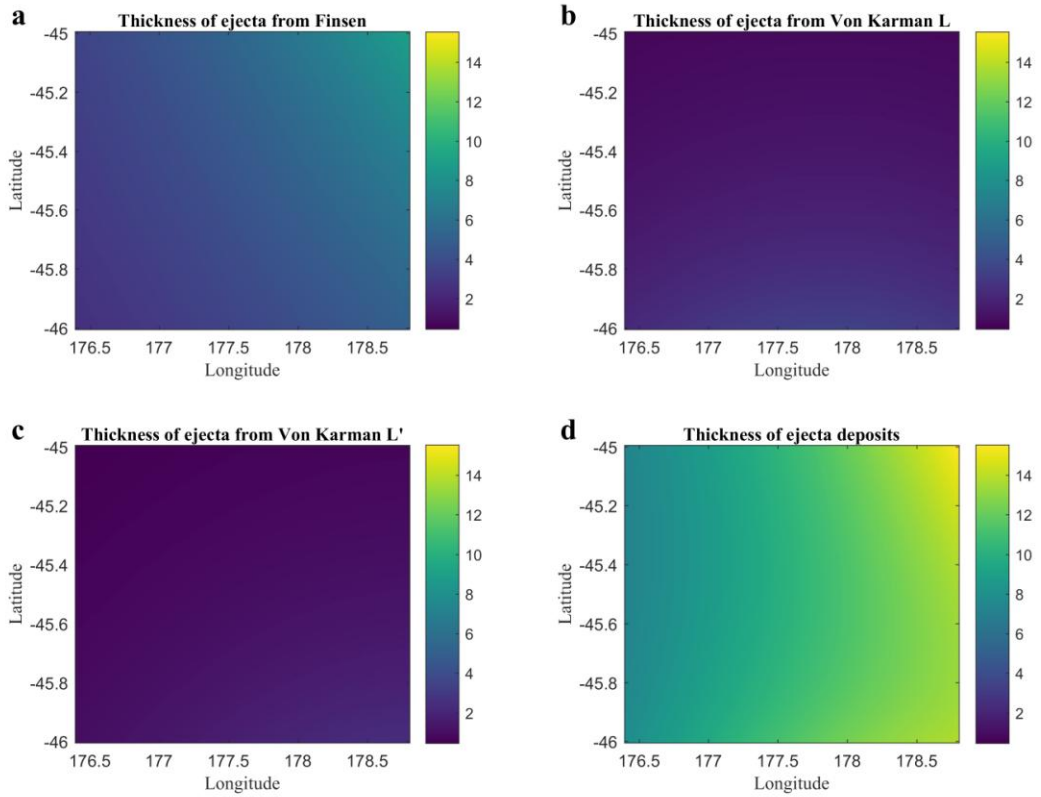

Fig. 10 The thickness of ejecta from a) Finsen crater, b) Von Kármán L crater, and c) Von Kármán L' crater. d) Thickness of all ejecta deposits consisting of excavated local material and accumulated ejecta from Finsen, Von Kármán L and Von Kármán L'. The location of (a), (b), (c), (d) is labeled in Fig. 1d.